AFRL-RX-WP-TR-2022-0043

HIGH-SPEED LOW NOISE SHORT-WAVELENGTH INFRARED TYPE II SUPERLATTICE HETEROJUNCTION PHOTOTRANSISTORS

Manijeh Razeghi
Northwestern University

28 April 2022
Final Report

**AIR FORCE RESEARCH LABORATORY
MATERIALS AND MANUFACTURING DIRECTORATE
WRIGHT-PATTERSON AIR FORCE BASE, OH 45433-7750
AIR FORCE MATERIEL COMMAND
UNITED STATES AIR FORCE**

NOTICE AND SIGNATURE PAGE

Using Government drawings, specifications, or other data included in this document for any purpose other than Government procurement does not in any way obligate the U.S. Government. The fact that the Government formulated or supplied the drawings, specifications, or other data does not license the holder or any other person or corporation; or convey any rights or permission to manufacture, use, or sell any patented invention that may relate to them.

Qualified requestors may obtain copies of this report from the Defense Technical Information Center (DTIC) (http://www.dtic.mil).

AFRL-RX-WP-TR-2022-0043, HAS BEEN REVIEWED AND IS APPROVED FOR PUBLICATION IN ACCORDANCE WITH ASSIGNED DISTRIBUTION STATEMENT.

EYINK.KURT.G.1230122136 Digitally signed by EYINK.KURT.G.1230122136 Date: 2022.05.16 15:54:23 -04'00'

KURT EYINK
Program/Project Manager/Engineer
Nanoelectronic Materials Branch
Functional Materials Division
Materials and Manufacturing Directorate

SCHMITT.MARK.G.1257789701 Digitally signed by SCHMITT.MARK.G.1257789701 Date: 2022.05.17 13:53:40 -04'00'

MARK SCHMITT
Branch Chief
Nanoelectronic Materials Branch
Functional Materials Division
Materials and Manufacturing Directorate

This report is published in the interest of scientific and technical information exchange, and its publication does not constitute the Government's approval or disapproval of its ideas or findings.

REPORT DOCUMENTATION PAGE

Form Approved
OMB No. 0704-0188

1. REPORT DATE *(DD-MM-YY)*	2. REPORT TYPE	3. DATES COVERED *(From - To)*
28 April 2022	FINAL	30 November 2017 – 30 June 2022

4. TITLE AND SUBTITLE
High-speed Low-noise Short Wavelength Infrared Type-II Superlattice Heterojunction Phototransistors

5a. CONTRACT NUMBER
FA8650-18-1-7810

5b. GRANT NUMBER

5c. PROGRAM ELEMENT NUMBER
DARPA

6. AUTHOR(S)
Manijeh Razeghi

5d. PROJECT NUMBER

5e. TASK NUMBER

5f. WORK UNIT NUMBER
X1ES

7. PERFORMING ORGANIZATION NAME(S) AND ADDRESS(ES)
Northwestern University
220 Campus Drive,
Cook Hall, Room #4051
Evanston, IL 60208-0893

8.PERFORMING ORGANIZATION REPORT NUMBER.

9. SPONSORING/MONITORING AGENCY NAME(S) AND ADDRESS(ES)
Air Force Research Laboratory
Materials and Manufacturing Directorate
Wright-Patterson Air Force Base, OH 45433-7750
Air Force Materiel Command
United States Air Force

10. SPONSORING/MONITORING AGENCY ACRONYM(S)
AFRL/RXAN

11. SPONSORING/MONITORING AGENCY REPORT NUMBER(S)
AFRL-RX-WP-TR-2022-0043

12. DISTRIBUTION/AVAILABILITY STATEMENT:
DISTRIBUTION STATEMENT A. Approved for public release; distribution is unlimited.

13. SUPPLEMENTARY NOTES
Document contains color.

14**. ABSTRACT** (To date, most optical receiver designs have employed pin photodiodes as photodetectors. However, these devices exhibit no internal/intrinsic gain, and the increased capacitance due to their relatively large-area intrinsic absorption layer is known to be the limiting factor for high frequency operation of the photoreceiver. Heterojunction phototransistors (HPTs) are an alternative technology that can demonstrate both high speed and internal gain. Functionally, a HPT is a pin photodiode integrated with a bipolar transistor to form an integrated amplifier. Unlike avalanche photodiodes (APDs), HPTs can provide large photocurrent gain without requiring high bias voltages or the excess avalanche noise characteristic of avalanche photodiode operation. Furthermore, HPTs are well suited to integration with heterojunction bipolar transistors in receivers or other circuits. It is, therefore, expected that HPTs will provide an exciting alternative for the manufacture of optical receivers and high-sensitivity imagers at wavelengths longer than 1.55 μm. A type-II superlattice (T2SL) material system and design can be a promising alternative for HPT SWIR devices. T2SLs are a developing material system that has led to the development of high performance HPTs. The T2SL-based HPTs can also be a possible solution to the urgent demand for sensitive and high speed photodetectors. In this project, the temperature dependence performance of SWIR T2SLs-based HPT device for different size have been investigated and demonstrated for the first time in the world. The novel device structure, world's first SWIR resonant cavity enhanced heterojunction phototransistor based on type-II superlattices grown by MBE has been demonstrated. The high performance MWIR HPT devices based on T2SLs have also been developed for the first time in the world. We also demonstrated the design, growth, and characterization of the world's first high-gain band-structure-engineered LWIR heterojunction phototransistor based on type-II superlattices. The optical gain of the device at 77 K saturates at a value of 276 at an applied bias of 220 mV, which is the highest record reported in the world.)

15. SUBJECT TERMS Microwave photonics, optical receiver, short wavelength infrared, heterojunction phototransistor, type-II superlattice, molecular beam epitaxy, optical gain, high frequency, resonant cavity structure, band structure engineering.

16. SECURITY CLASSIFICATION OF:			17.LIMITATION OF ABSTRACT:	18. NUMBER OF PAGES	19a. NAME OF RESPONSIBLE PERSON (Monitor)
a. REPORT	b. ABSTRACT	c. THIS PAGE			Kurt Eyink
Unclassified	Unclassified	Unclassified	SAR	34	19b. TELEPHONE NUMBER *(Include Area Code)* (937) 255-5710

TABLE OF CONTENTS

LIST OF FIGURES

Figure **Page**

LIST OF TABLES

Table **Page**

1. SUMMARY

Most of the optical receiver designs have employed pin photodiodes as photodetectors. However, these devices exhibit no internal/intrinsic gain, and the increased capacitance due to their relatively large-area intrinsic absorption layer is known to be the limiting factor for high frequency operation of the photoreceiver. Heterojunction phototransistors (HPTs) are an alternative technology that can demonstrate both high speed and internal gain. Functionally, a HPT is a pin photodiode integrated with a bipolar transistor to form an integrated amplifier. Unlike avalanche photodiodes (APDs), HPTs can provide large photocurrent gain without requiring high bias voltages or the excess avalanche noise characteristic of avalanche photodiode operation. Furthermore, the HPTs are well suited to integrate with heterojunction bipolar transistors in receivers or other circuits. It is, therefore, expected that HPTs will provide an exciting alternative for the manufacturing of the optical receivers and high-sensitivity imagers at wavelengths longer than 1.55 μm. A type-II superlattice (T2SL) material system and design can be a promising alternative for HPT SWIR devices. T2SLs are a developing material system that has led to the development of high performance HPTs. The T2SL-based HPTs can also be a possible solution to the urgent demand for sensitive and high speed photodetectors. In this project, the temperature dependence performance of SWIR T2SLs-based HPT device for different size have been investigated and demonstrated for the first time in the world. The novel device structure, world's first SWIR resonant cavity enhanced heterojunction phototransistor based on type-II superlattices grown by MBE has been demonstrated. The high performance MWIR HPT devices based on T2SLs have also been developed for the first time in the world. We also demonstrated the design, growth, and characterization of the world's first high-gain band-structure-engineered LWIR heterojunction phototransistor based on type-II superlattices. The optical gain of the device at 77 K saturates at a value of 276 at an applied bias of 220 mV, which is the highest record reported in the world.

2. INTRODUCTION

Microwave photonics is an interdisciplinary area that studies the interaction between microwave and optical signals, for applications such as broadband wireless access networks, sensor networks, radar, LIDAR, satellite communications, instrumentation, and warfare systems. In the past few years, there has been an increasing effort in researching new microwave photonics techniques for different applications. The major functions of microwave photonics systems include photonic generation, processing, control, distribution, and detection of microwave and millimeter-wave (mm-wave) signals. In general, the topics covered by microwave photonics include photonic generation of microwave and mm-wave signals, photonic processing of microwave and mm-wave signals, optically controlled phased array antennas, radio-over-fiber systems, and photonic analog-to-digital conversion.

The performance of microwave and millimeter-wave photonic systems would benefit from the use of photodetectors with high sensitivity, high speed, and high responsivity performance. The current state-of-the-art microwave photonic systems is based around the use of near-infrared (NIR, $0.7 < \lambda < 1.55$ μm) sources and photodetectors. Moving from the NIR towards the longer wavelengths (1.55 μm $< \lambda$) allows superior transmission through common atmospheric problems such as fog, clouds, and smoke. This is driving a new demand for fast and sensitive infrared photodetectors at wavelengths longer than 1.55 μm. However, photodetector performance in those regions is still behind the requirements of LIDAR, free-space optical communications, and other microwave photonic applications. Achieving suitable performance will require developing a novel solution that can overcome current device limitations.

To date, most optical receiver designs have employed *pin* photodiodes as photodetectors. However, these devices exhibit no internal/intrinsic gain, and the increased capacitance due to their relatively large-area intrinsic absorption layer is known to be the limiting factor for high frequency operation of the photoreceiver. Heterojunction phototransistors (HPTs) are an alternative technology that can demonstrate both high speed and internal gain. Functionally, a HPT is a pin photodiode integrated with a bipolar transistor to form an integrated amplifier. Unlike avalanche photodiodes (APDs), HPTs can provide large photocurrent gain without requiring high bias voltages or the excess avalanche noise characteristic of avalanche photodiode operation. Furthermore, HPTs are well suited to integration with heterojunction bipolar transistors in receivers or other circuits. It is, therefore, expected that HPTs will provide an exciting alternative for the manufacture of optical receivers and high-sensitivity imagers at wavelengths longer than 1.55 μm.

A type-II superlattice (T2SL) material system and design can be a promising alternative for HPT SWIR devices. T2SLs are a developing material system that has led to the development of high performance HPTs. The T2SL-based HPTs can also be a possible solution to the urgent demand for sensitive and high-speed photodetectors.

A heterojunction phototransistor (HPT) consists of the integration of a photodiode and a bipolar junction transistor (BJT) preamplifier into one device. We design e-SWIR base design, where the emitter consists of a large-bandgap superlattice based on M-structure. The device has two terminals and the base region is not connected to any terminal. We created a set up for temperature dependence high-speed test of SWIR HPT, which was introduced in Chapter 3. The optical and electrical performance of the eSWIR device along with the paper that we published about it was reported.[1] Then the investigation on the effect of different parameters such as emitter doping, base thickness and bandgap offset, etc on the HPT performance was performed

and reported.[2, 3]. We developed an resonant cavity enhanced heterojunction phototransistor based on InAs/GaSb/AlSb type-II superlattice and the device showed the wavelength selectivity and a cavity enhancement of the responsivity at 1.9 μ m at room temperature.[4]

3. GAIN MECHANISM VIA CHARGE TRANSMISSION IN HIGH OPTICAL GAIN HPT E-SWIR HPTS

A heterojunction phototransistor (HPT) consists of the integration of a photodiode and a bipolar junction transistor (BJT) preamplifier into one device. Figure 1 presents the design structure and fabrication method of e-SWIR HPT device. This structure has a floating base with only two external terminals—the photodetector is integrated directly into the collector and coupled directly to the base without the need for an external contact to bias the base. This floating base structure allows the incident light to directly illuminate the collector and base region of the HPT and greatly simplifies the device design and processing. The e-SWIR light is absorbed in the narrower bandgap base and collector regions where it leads to the generation of electron-hole pairs. These generated electron-holes in base-collector region are swept to the base-collector junction by the built-in field; they are also separated according to the diffusion lengths of the minority carriers in the base (*p-type*) and collector (*n-type*).

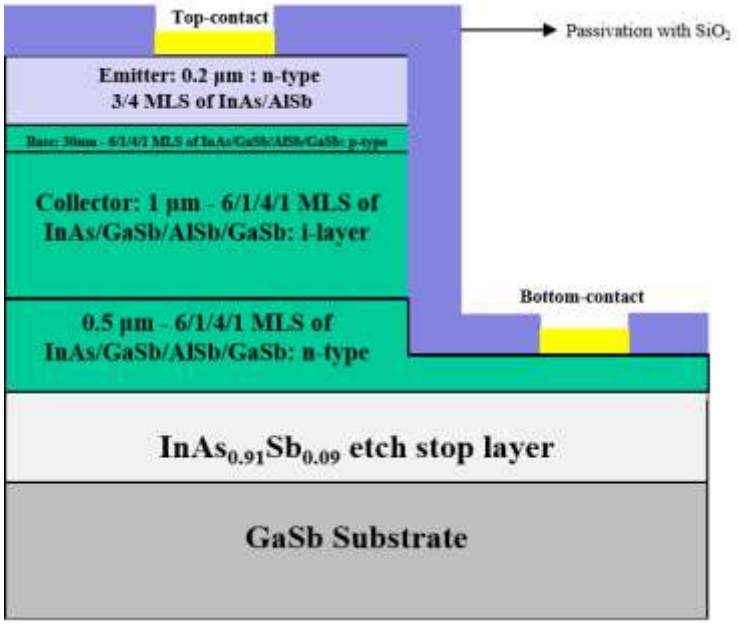

Figure 1. Schematic of the HPT design and structure and fabrication method. The incident light is absorbed in SWIR T2SL-based collector regions, creating electron-hole pairs.

The large potential barrier in the valence band at the emitter-base junction blocks the holes to get in the emitter and creates accumulation of the holes in the base until they recombine with injected electrons from the emitter. Accumulation of photo-generated holes in the base region controls the potential level of the base and increases the forward bias of the emitter-base junction. In an appropriate emitter-collector bias voltage, electrons are injected from the emitter into the base crossing the base toward the collector region. To maintain charge-neutrality in the base, a large injection of electrons occurs from the emitter into the base resulting in a large electron-current flow from the emitter to the collector. When the emitter-base junction is forward biased, a wide-bandgap emitter can provide emitter-base injection efficiency close to unity,

regardless of the relative base/emitter doping levels since the valence-band barrier effectively prevents hole injection from base to the emitter.[1]

A series of eSWIR HPT devices were designed and grown. All the HPT devices share the similar material structure, which is shown in Fig.2. These devices adopt a two-terminal design without the base contact, which make the device design and fabrication simpler. These devices all consist of a six-layered structure (from the bottom to top): (a) a GaSb substrate, (b) the InAsSb buffer layer, (c) an n-doped M-structure T2SL-based contact layer, (d) an T2SL-based collector without intentionally doping and the collector thickness (1.0 μm) is the same for all the samples, (e) a p-doped base layer, (f) an n-doped InAs/AlSb T2SL-based emitter and the emitter thickness (0.2 μm) is the same for all the samples. The same superlattice design, 6/1/4/1 monolayers (MLs) of InAs/GaSb/AlSb/GaSb is adopted for the base, collector, and the contact layer and the energy bandstructure of the device was shown in Fig.2 (b).

All the HPT structures in this study were grown by solid source molecular beam epitaxy (MBE). During the growth, different device parameters were varied to fulfill the different HPT device designs. For example, the effusion cell temperature of n-type dopant （p-type dopant） was changed to have the emitter (base) with different doping concentration. The growth time for the base layer was varied to get different thickness base. Two different superlattice designs were adopted for the emitter to tune the bandgap difference between the emitter and base (ΔEg).

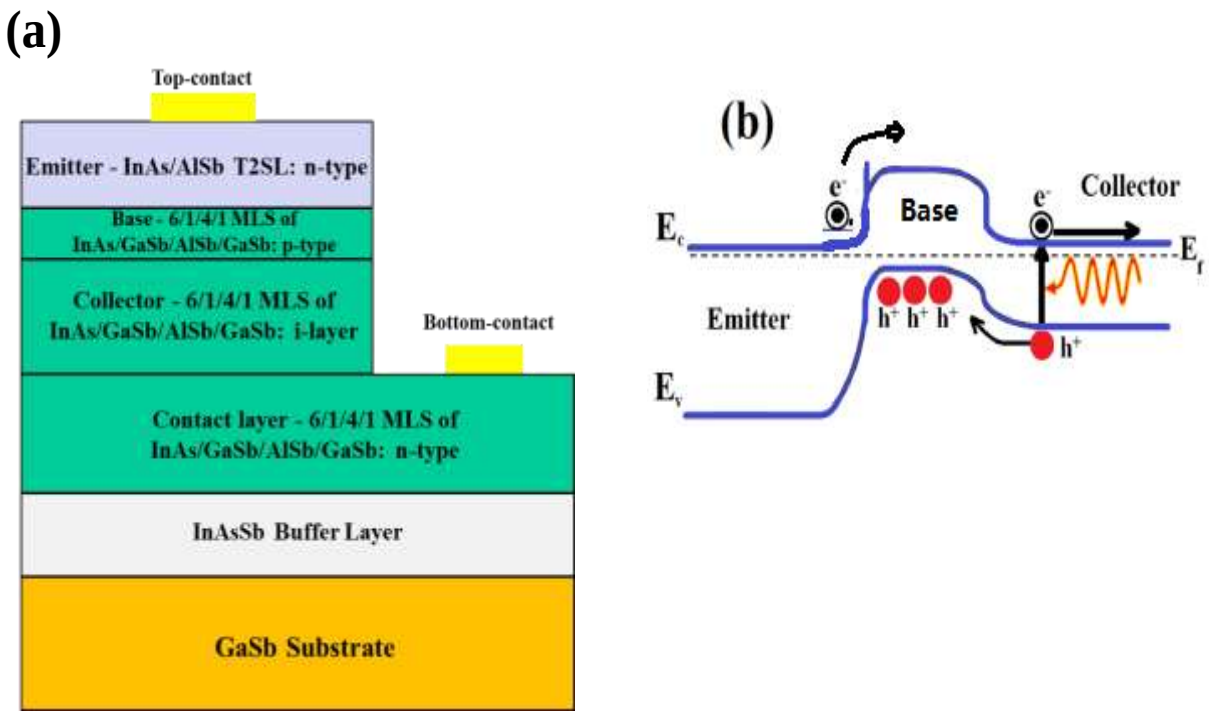

Figure 2. (a) The basic material structure of all the HPT devices in this study. (b) The energy band structure of the HPT devices.

After growth, all the samples were fabricated into the HPT devices using our standard phototransistor fabrication steps, which can be found elsewhere.[5] All the HPTs were left

unpassivated but were cleaned thoroughly during processing to minimize the dark current. Then the absolute responsivity of all the HPT devices were measured at room temperature using the calibrated blackbody source at 1000 ℃. Their optical gains (G) were calculated by the following expression:

$$G = 1.24R / \lambda$$

Where, R is the responsivity of the HPT device, and λ is the wavelength in micrometers. The optical gains of the HPT samples with different device designs were then compared to analyze the effect of the device parameters.

The effect of emitter doping concentration on optical gain was investigated by using difference doping cell temperatures. During the MBE growth, different Si effusion cell temperatures from 1050 ℃ to 1120 ℃ were adopted to achieve different emitter doping concentration for sample A1, A2 and A3. The other device parameters were kept as the same and are listed in Table 1.

Table 1. The device parameters of sample A1, A2 and A3 with different emitter doping concentration.

Sample No.	Emitter superlattice design	Emitter doping concentration (cm^{-3})	Base doping concentration (cm^{-3})	Base thickness (nm)
Sample A1	3/4 MLs InAs/AlSb T2SL	9.6E16	2.1E17	30
Sample A2	3/4 MLs InAs/AlSb T2SL	1.5E17	2.1E17	30
Sample A3	3/4 MLs InAs/AlSb T2SL	2.3E17	2.1E17	30

The responsivity of the three samples were measured at a bias voltage of 3.5 V and their optical gains were calculated, which are shown in Fig.3.

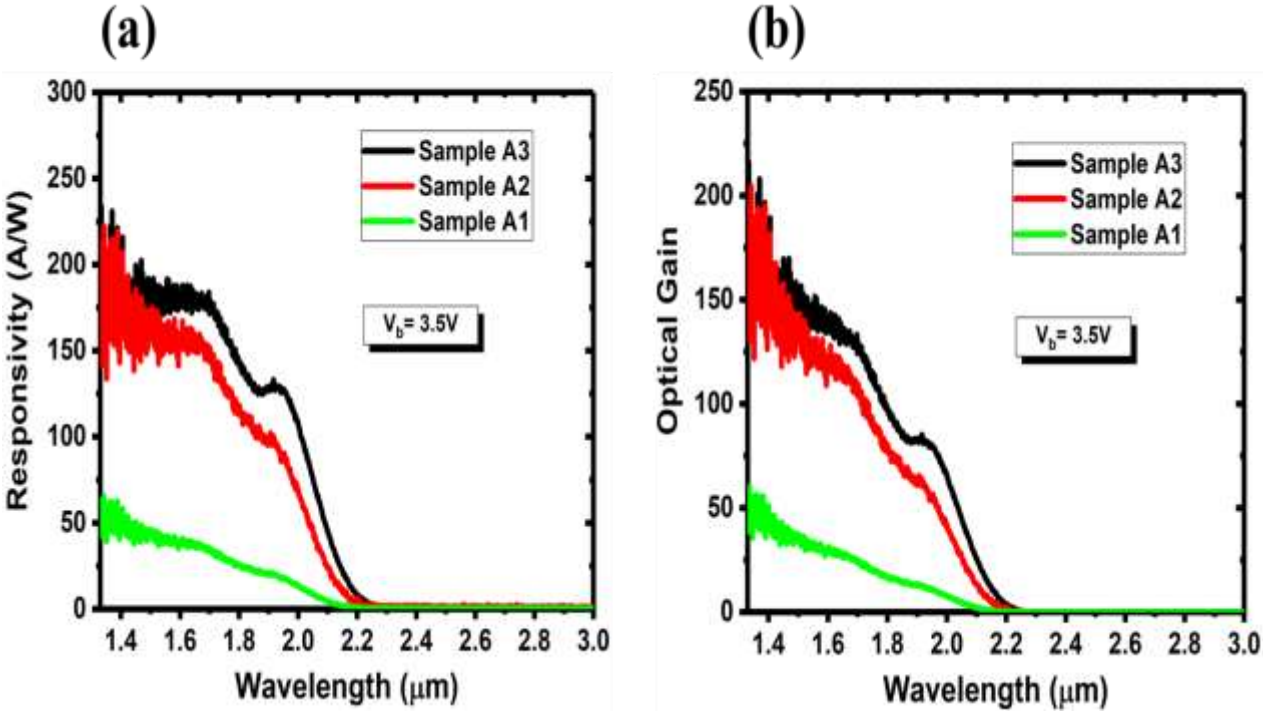

Figure 3. (a) The responsivity and (b) the optical gain of the three samples with different emitter doping concentration.

The responsivity increases from 39.14 A/W to 183.15 A/W at 1.6 μm while the emitter doping concentration increases from 9.6×1016 cm-3 to 2.3×1017 cm-3, as shown in Fig.3(a). The optical gains of the HPTs follow the same trend, increasing from 29.8 to 140.9 when the emitter doping concentration increases. The increase is due to the higher ratio of emitter doping concentration to the base doping concentration, which can improve the emitter injection efficiency. However, when the ratio of emitter doping concentration to the base doping concentration is high enough, the emitter injection efficiency will approach unity, leading to the saturated current and optical gain. Therefore, the optical gain between sample A2 and A3 only changes from 121.5 to 140.9.

For the HPTs based on conventional materials, the emitter doping concentration always has an impact on the electrical performance of HPTs. The same behavior was observed in the comparison between the electrical performances of samples A1-A3, which is shown in Fig. 4. At room temperature, the dark current of sample A3 with higher emitter doping concentration at 3.5 V is ~49.7 A/cm^2, about two orders of magnitude higher than the dark current of sample A1 at

3.5 V (~0.34 A/cm^2), which is due to the larger tunneling current caused by the higher emitter doping concentration.

-

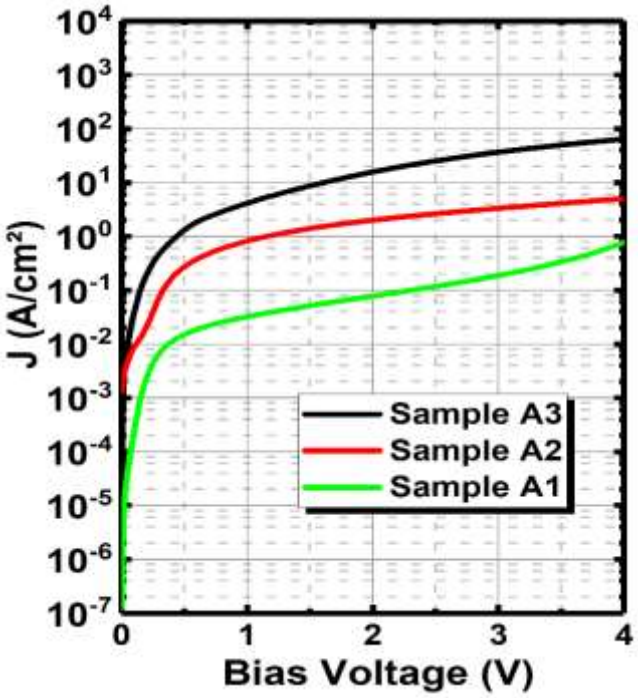

Figure 4. The dark current of sample A1-A3 vs. voltage at room temperature.

4. DESIGN AND GROWTH OF THE E-SWIR HPTS DEVICE FOR HIGH SPEED APPLICATIONS

The designed high-speed HPT device consists of n-doped wide-bandgap emitter, a lightly doped n-type e-SWIR collector—both T2SL-based—and a simple p-doped GaSb base (5a). The emitter superlattice design consists of 3/4 mono-layers (MLs) of InAs/AlSb, respectively, per period with a ~760 meV bandgap. The collector regions consist of 5/1/5/1 MLs of InAs/GaSb/AlSb/GaSb, respectively with one interface being binary InSb and the other interface being InGaSb to reduce the strain. This collector superlattice has a ~580 meV bandgap. The conduction band offset between emitter and base is ~ 250 meV and the valence band discontinuity is ~ 200 meV.

The material for this HPT was grown in an Intevac GEN-II solid-source molecular beam epitaxy (SSMBE) reactor on a Te-doped *n*-type (10^{17} cm^{-3}) GaSb wafer. The growth started with a 100 nm GaSb buffer layer to stabilize the wafer surface, then, a 500 nm *n*-doped $InAs_{0.91}Sb_{0.09}$ etch stop layer (10^{18} cm^{-3}). Then an *n-type* (10^{18} cm^3) 0.5 μm-thick bottom contact layer was grown using the same superlattice design as the emitter. Then, the 0.25 μm-thick wide-bandgap *n*-doped (10^{16} cm^3) emitter was grown. A lower doping level at the emitter can help provide a thick emitter–base depletion region and reduce the depletion capacitance. The subsequent growth were a 40 nm-thick *p*-doped GaSb base layer (10^{15} cm^3), the 0.1 μm-thick *n*-doped collector/absorption region (10^{16} cm^3), and finally the 0.5 μm *n*-type top contact (10^{18} cm^3). The top contact has the same superlattice design as the collector region. Silicon was used as the *n*-type dopant, and beryllium was used as the *p*-type dopant. After epitaxial growth, the material quality was evaluated by high-resolution X-ray diffraction (HR-XRD) and atomic force microscopy (AFM). The lattice mismatch between both superlattice designs and the GaSb substrate was less than 1000 ppm. AFM showed a smooth, well-ordered, surface with the roughness of 0.16 μm over a 10 μm × 10 μm area.

We set up our measurement system to achieve high-speed RF measurements for the HPT devices. Figure 7 presents schematic diagram of the high frequency measurement setup. The sample G-S-G contact layout is connected by a G-S-G microwave probe wired to a bias-tee, which allows a DC bias voltage to be applied at the same time as allowing measurement of the RF signal using a spectrum analyzer. To measure the optical frequency response of the phototransistor, a RF signal generator with variable frequency is connected to the modulation input of an electro-optical converter, which has a 1.55 μm laser inside. Then the 1.55 μm obliquely illuminates the phototransistor at a 45° angle via a fiber-optic probe. More details about our high-speed testing system set up can be found elsewhere.[6, 7] The HPT samples were loaded into a microwave probe station at room temperature. A 40 GHz G-S-G microwave probe was then connected electrically to the phototransistor via a bias tee.

The processing high-speed HPT samples has different mesa geometry, contact geometry and a radio frequency (RF) capable ground-signal-source (GSG) layout strip line to allow for high-speed measurements. The process starts with the standard lithography to define circular mesas with smaller diameters ranging from 10 to 100 μm. These were etched and cleaned in the same way as the single element photodetectors.

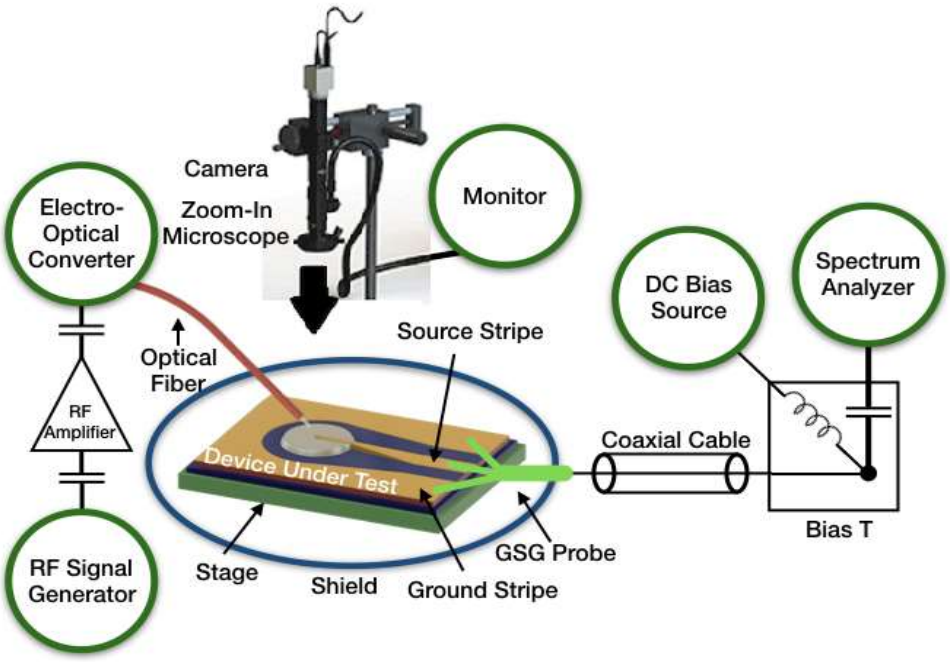

Figure 5. Schematic diagram of high frequency measurement setup. The sample GSG contact layout is connected by a GSG microwave probe, which is wired to a bias-tee, which allows applying a DC bias voltage at the same time as measuring the AC current thanks to a spectrum analyzer. The sample is illuminated with a RF signal generator and an electro-optical converter through an optical fiber at a 45° angle.

Top and bottom ohmic contacts consisting of 40 nm/300 nm/10 nm Ti/Au/Ti were then deposited via negative lithography and electron beam evaporation. The bottom contact was designed to be close to the border of the mesa in order to decrease the series resistance of the diode. The high-speed HPT sample was then additionally passivated with a 1.5 µm thick SiO_2 layer that was deposited via plasma enhanced chemical vapor deposition (PECVD). Windows to the top and bottom contacts were then opened through the SiO_2 layer via electron cyclotron resonance (ECR) reactive ion etching in a CF4 plasma. Finally, 80 nm/400 nm Ti/Au strip lines were deposited on the sample from the top and bottom contacts in order to interface with a GSG microwave probe. Sample was then loaded into a microwave probe station for room temperature operation. A GSG microwave probe with a frequency cutoff higher than 40 GHz connects the diode to a spectrum analyzer via a bias-tee rated for up to ~20 V_{DC} and frequencies from 20 kHz to 26.5 GHz.

Figure 6 displays microscope images of the sample during different steps of processing and SEM images of final devices with different mesa diameters (30µm and 15 µm) ready for RF measurements.

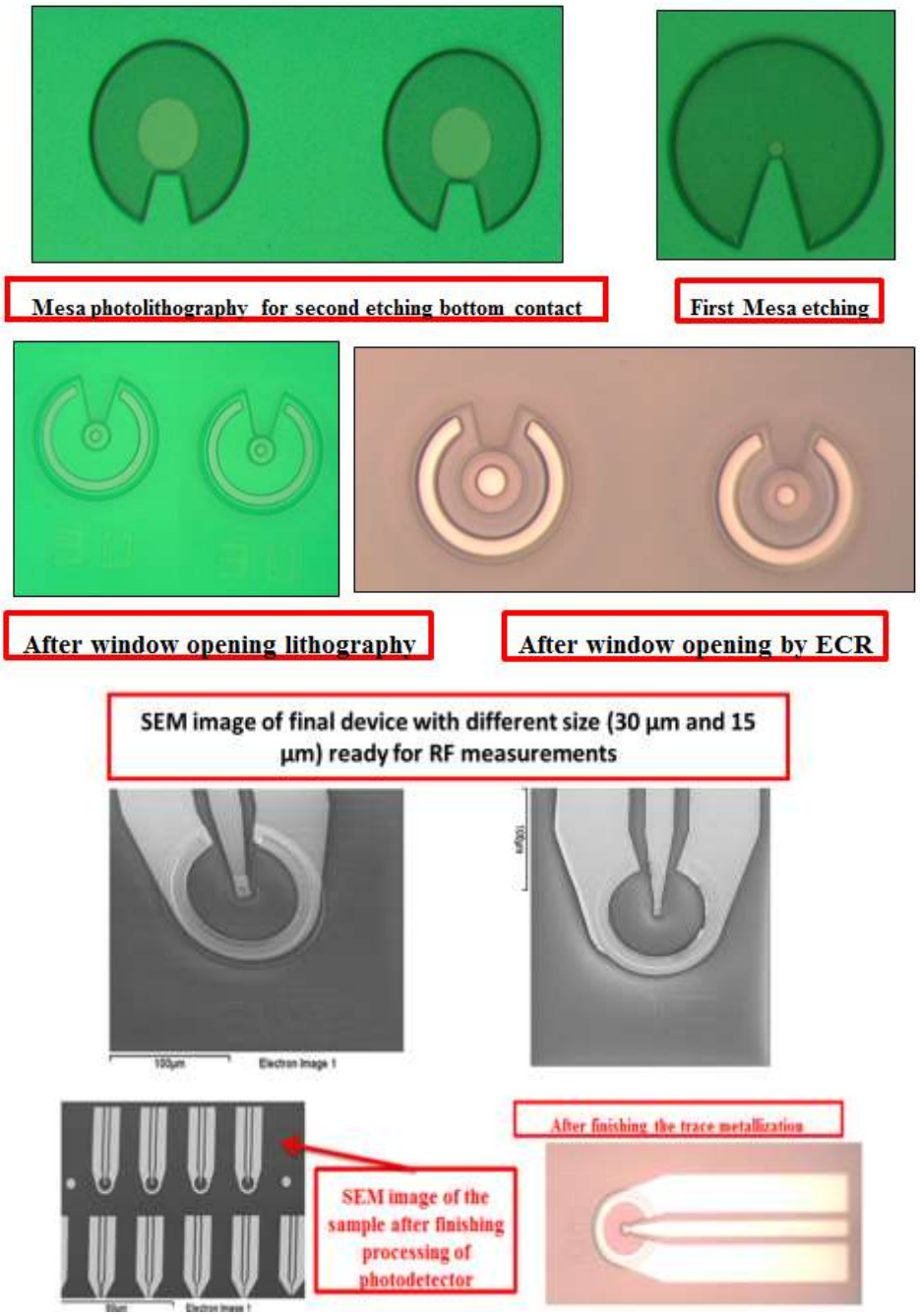

Figure 6. Microscope image of the sample during different step of processing and SEM image of final device with different mesa diameter (30µm and 15 µm) ready for high-speed measurements.

We created a new set up for testing the temperature dependence of the high-speed behavior of the SWIR HPT. We performed RF characterization at different temperatures for e-SWIR HPT device and ~~we~~ get the highest speed for an HPT so far.

As shown in Figure 7, a stage equipped with temperature controller and cooling system was developed to test the temperature dependence of the high-speed behavior of the SWIR HPTs.

The samples were put on the stage and their high-speed performance was tested at different temperature to study the effect of different temperature. The lowest temperature we were able to test devices with our cooling system at 250K.

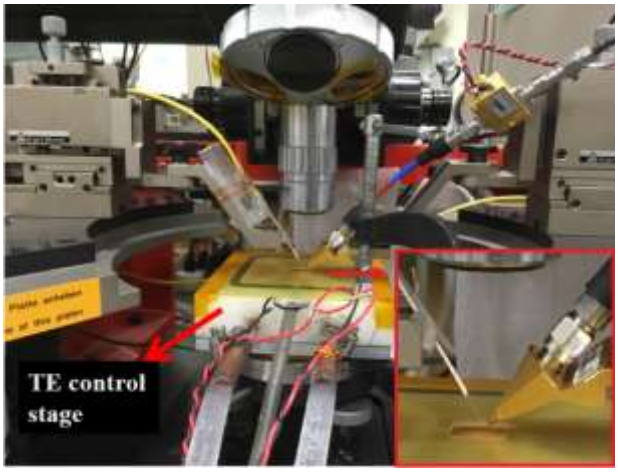

Figure 7. The measurement set up with a new stage designed for temperature dependence high speed test of SWIR HPT equipped with temperature controller.

Figure 8 presents normalized frequency response for the HPT e-SWIR device at different temperature spanning from 350 down to 250K. The diode size is 15µm diameter circular photodetectors under -20V applied bias. For this sample, the -3dB cut-off frequency for devices having a 15 µm diameter circular diode was about 1.5 GHz -3dB, at room temperature with -20 V bias voltage. At 250K, the results showed that the speed marginally improved to 1.8 GHz probably due to lower dark current but was not significantly higher than room temperature. Also, we tested the device at higher temperature of 350 K, where no significant change in speed performance of the device was seen. The summary of cut-off frequency for all the devices at -3dB is given in Table 2, where the 3db cut-off frequency increases when the measurement temperature decreases from 300 K to 250 K.

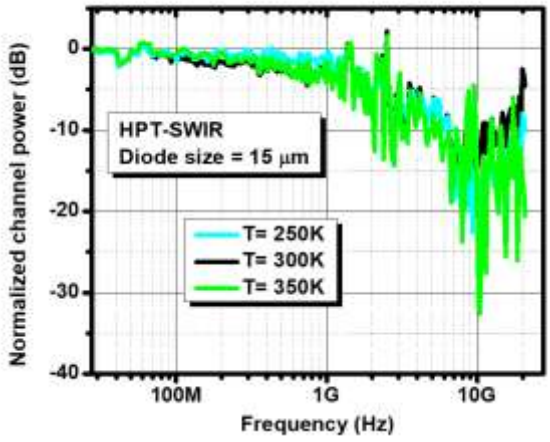

Figure 8. Normalized frequency response for the HPT e-SWIR device at different temperature. The diode size is 15µm diameter circular photodetectors under -20V applied bias.

Table 2. Summary of -3dB cut-off frequency for HPT e-SWIR devices with 15µm diameter size and -20V applied bias.

Temperature	f_{3db}	Size
T= 250 K	1.8 GHz	15 µm
T= 300 K	1.5 GHz	15 µm
T= 350 K	1.5 GHz	15 µm

Lateral scaling can improve high-speed performance of a photodetector. We previously have presented the impact of lateral scaling for e-SWIR *p-i-n* photodetector and reported that the cut-off frequency increases when the diode diameter decreases.[7] A portion of this increase in speed is attributed to the reduction in photodetector capacitance and the associated R-C time constant, which increases in proportion of the inverse of the diode area. In order to examine the same phenomena, we performed the temperature dependent high-speed test on a photodetector with a different diode diameter of 10 µm.

Figure 9 presents normalized frequency response for the HPT e-SWIR device for the diode size of 10µm diameter under -20V applied bias at different temperature spanning from 300 down to 250K. For this device, the -3dB cut-off frequency for 10 µm diameter circular diode was about 1.8 GHz -3dB, at room temperature with -20 V bias voltage.

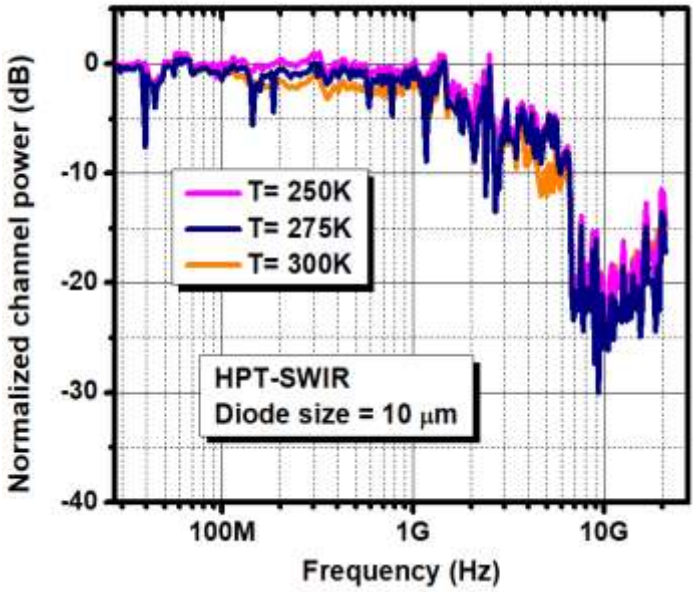

Figure 9. Normalized frequency response for the HPT e-SWIR device at different temperature. The diode size is 10µm diameter circular photodetectors under -20V applied bias.

At the lowest temperature of 250K, the speed improved a bit up to 2.2 GHz, probably due to lower dark current at low temperature. In general, the device performance is not significantly changing over the temperatures studied.

The summary of cut-off frequency for all the 10 µm devices at -3dB is demonstrated in Table 3, the -3 dB cut-off frequency increases from 1.8 GHz to 2.2 GHz when the temperature decreases from 300 K to 250 K.

Table 3. Summary of -3dB cut-off frequency for HPT e-SWIR devices with 10µm diameter at -20V applied bias.

Temperature	f_{3db}	Size
T= 250 K	2.2 GHz	10 µm
T= 275 K	2.0 GHz	10 µm
T= 300 K	1.8 GHz	10 µm

By scaling the lateral size of the photodetector we can optimize the device performance. Compare the device performance in Table 2 and 3. This could be considered the promising approach for enhancing the performance of e-SWIR HPT devices. As we noticed lateral scaling the active region can improve the speed of the device. For scaling the size, the electron beam lithography can be used to create super small diode size for e-SWIR HPT devices based on T2SLs.

5. THE RESONANT CAVITY ENHANCED HPT STRUCTURE

In our research, the trade-off between strong photo response and high-speed performance in terms of the absorption/collector layer thickness of the type-II superlattice based HPT device has been found and investigated. The trade-off between collector thickness and responsivity can be broken if the active layer is placed in a resonant cavity that offers multiple passes of the incident light. In such a structure, the effective optical path in the collector layer will become longer without making it thicker. So, it is promising to improve the high-speed performance of T2SL based HPT with thinner collector layer while not degrading the responsivity.

Fig. 10. shows the designed RCE-HPT structure grown by MBE. The RCE-HPT design can be divided into three parts including the optical cavity, top and bottom mirrors. The optical cavity length, L, which is also the total thickness of the active layer is designed to satisfy the cavity resonance condition at resonant wavelength of 1.9 μm. The interface between top epilayer and air is the top mirror and an eleven-pair GaSb-$AlAs_{0.08}Sb_{0.92}$ Bragg mirror stack is chosen as bottom mirror, which produces a high reflectivity. The thickness of GaSb and AlAsSb is 115 nm and 144 nm respectively, which achieve the required quarter-wavelength optical path length. The reflectivity of the eleven-pair GaSb-AlAsSb Bragg mirror stack can be calculated by the following formulation to be 99.2%.

$$R \approx 1 - 4\left(\frac{n_L}{n_H}\right)^{2P} \frac{n_S}{n_H^2}$$

Where R is the reflectivity, n_H and n_L are the indices of refraction of the high- and low-index films, P is the number of film pairs and n_S is the index of refraction of the substrate. The indices of refraction of GaSb and AlAsSb can be found in the previous reports. [8]

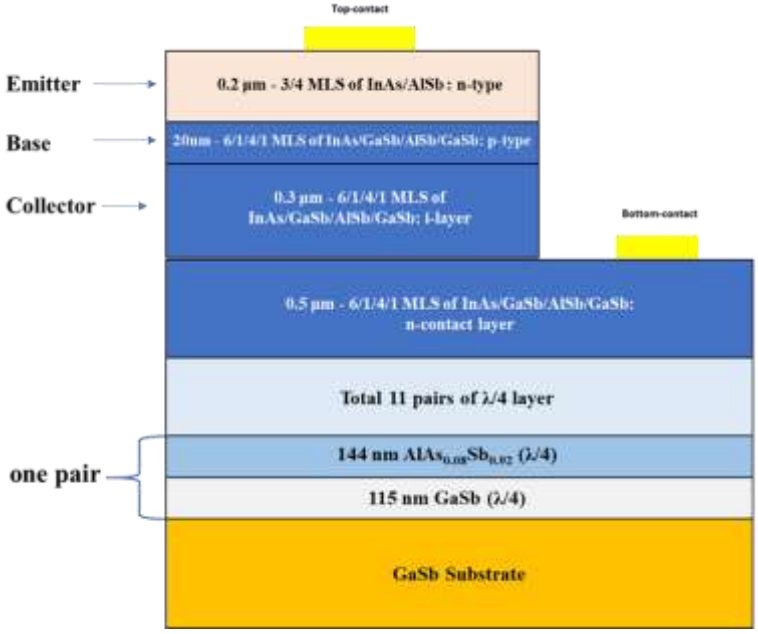

Figure 10. Design of the resonant cavity enhanced HPT (RCE-HPT) structure.

The RCE-HPT structure described above was then grown on a Te-doped n-type (10^{17} cm^{-3}) GaSb substrate using a GEN II molecular beam epitaxy (MBE) reactor. It is based on two-terminal n-p-n HPT design where a floating base is adopted. The growth started with a 200 nm GaSb buffer layer to stabilize the epilayer surface after deoxidation. Then, the bottom mirror, eleven pairs of GaSb (122 nm) and $AlAs_{0.08}Sb_{0.92}$ (152 nm) were grown. The AlAsSb layers were grown by digital alloy technique, which was used in the previous reports. After that, the optical cavity of a total thickness of ~0.76 μm was grown at a lower temperature than the bottom mirror layers. The cavity consists of an n-type 0.4 μm-thick bottom contact layer, an 80 nm-thick undoped collector, a 20 nm-thick p-doped base layer and an n-type 0.2 μm-thick emitter. The same M-structure superlattice design, 6/1/4/1 monolayers (MLs) of InAs/GaSb/AlSb/GaSb was adopted for bottom contact layer, collector, and base layer. A different superlattice design, 3/4 MLs of InAs/AlSb, which has a wider bandgap than the M-structure superlattice was used for the emitter to create a large potential barrier in the valence band at the emitter-base junction. The large potential barrier can result in high emitter injection efficiency and optical gain.

The RCE-HPT sample was then processed into a set of mesa-isolated devices via our standard T2SL photodetector processing steps.[9] The diode size ranges from 40×40 to 250×250 μm^2. After processing, the sample was wire-bonded and then loaded into a measurement system at room temperature (300K). The electrical performance was first tested by the semiconductor parameter analyzer. As shown in Fig. 11, the dark current density under 2.5 V bias voltage for the RCE-HPT device is 6.5×10^{-3} A/cm^2.

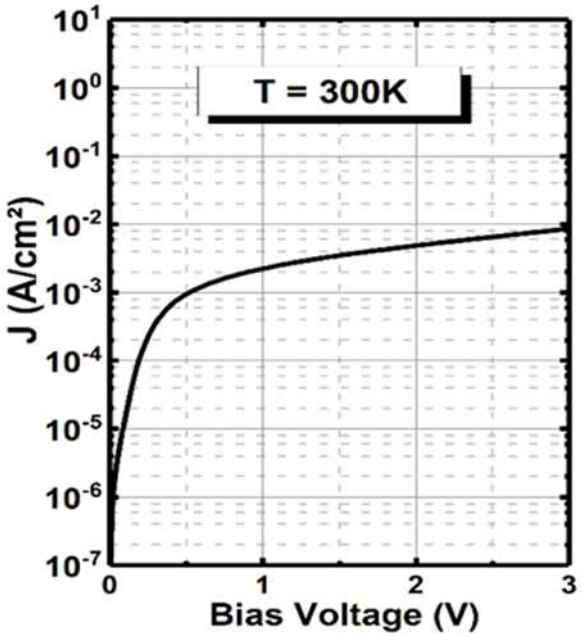

Figure 11. The electrical performance of the RCE-HPT sample.

Then the sample was illuminated from the top through the emitter to measure the spectral response and a calibrated 1000 ℃ blackbody source was used to calculate the responsivity. The

results, as shown in Fig. 12, confirm the 100% cut-off wavelength of the RCE-HPT sample at ~2.2 μm, which is consistent with the theoretical design. Figure. 12(a) depicts the spectral response of RCE-HPT device and relationship between the responsivity and bias voltage at room temperature. The responsivity spectra exhibit a sharp peak around 1.9 μm, with the associated fringes at the off-resonance wavelengths due to the resonant cavity effect. This indicates the GaSb/$AlAs_{0.08}Sb_{0.92}$ distributed Bragg reflector is effective, and has been grown correctly. The inset picture of Fig. 12(a) shows that for an 80 nm-thick absorption/collector layer by increasing the bias voltage, the responsivity of RCE-HPT increases and saturates above 2.5 V, reaching a peak value of 24.9 A/W at ~1.9 μm.

In order to establish baseline performance and meaningful comparison, another device with the same HPT design but without bottom Bragg mirror was grown and processed similar to the RCE-HPT device and used as a reference sample. The responsivity of RCE-HPT sample and the reference sample under applied bias of 2.5 V was compared to show intuitively the effect of the RCE structure, as shown in Fig. 12(b).

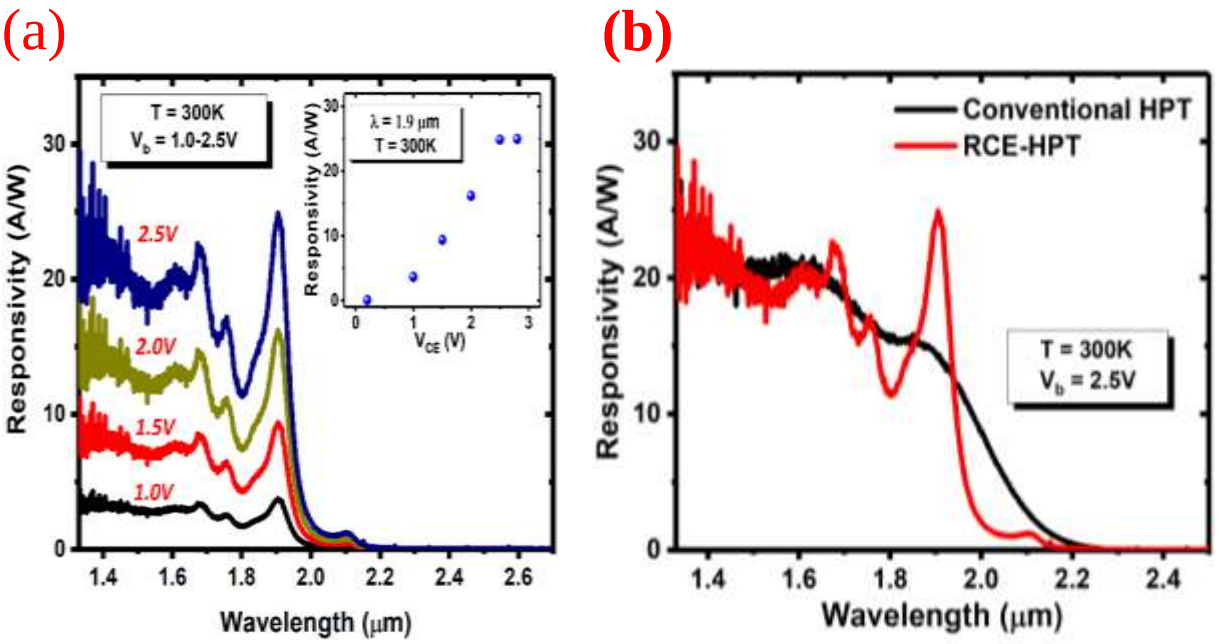

Figure 12. (a) The responsivity spectra of RCE-HPT under different bias voltage at 300K; the inset shows the variation of peak responsivity vs applied bias voltage. (b) The responsivity comparison between RCE-HPT and conventional HPT under applied bias of 3.0 V at 300K.

6. BAND-STRUCTURE-ENGINEERED HIGH-GAIN HPT BASED ON A TYPE-II SUPERLATTICE

Several HPT devices have been reported based on compound semiconductor material systems (such as InGaAs, InGaP, InP, and SiGe); these HPT devices exhibit large internal gain with high stability, and unlike APDs, they can operate at low bias voltages. However, these materials are limited to shortwave and near-infrared detection. One promising material that has shown the potential to push HPTs into the LWIR spectrum is type-II superlattices (T2SLs); HPT devices have already been reported that cover the extended short-wavelength and MWIR bands.

In this project, we explored a HPT structure which utilize the bandstructure engineering capabilities of InAs/GaSb and InAs/ GaSb/AlSb/GaSb T2SLs to realize the gain-based LWIR photodetetor. The exceptional band structure engineering capabilities of the T2SL material system allow each part of the device to be carefully tuned to achieve high optical gain, low noise, and high detectivity.

The high-gain LWIR photodetector device structure (Fig. 13) is based on an npn structure with a narrow bandgap InAs/GaSb n-type LWIR collector, a narrow bandgap InAs/GaSb p-type base, and a wide-bandgap InAs/GaSb/AlSb/GaSb n-type hybrid emitter.

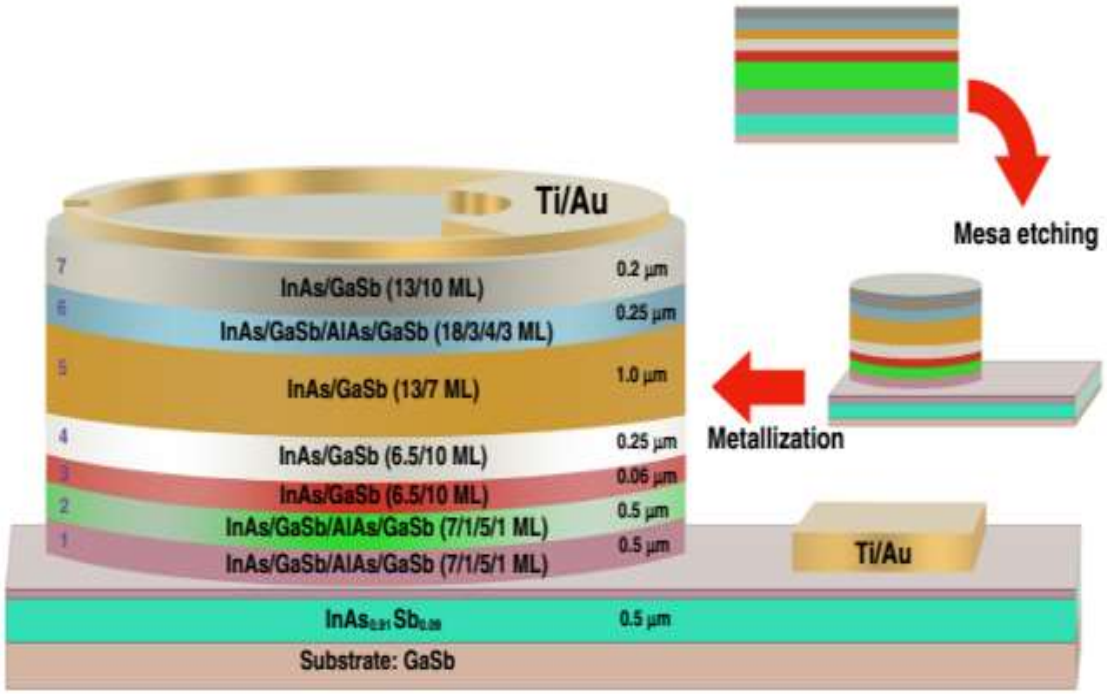

Figure 13. Schematic diagram of the LWIR T2SL phototransistor structure with a summary of the key fabrication steps at the right. Blue numbers indicate the sector designations used in Fig. 14, with 1 the bottom contact, 2 the emitter, 3 the base, and 4–5 the hybrid collector.

The empirical tight-binding method (ETBM) was used to design the constituent layers and calculate the band offsets (Fig. 14b). A schematic diagram of the conduction (E_C) and valence (E_V) bands of the LWIR photodetector device structure is presented in Fig. 14a, where sectors 1–7 are the different segments of the structure.

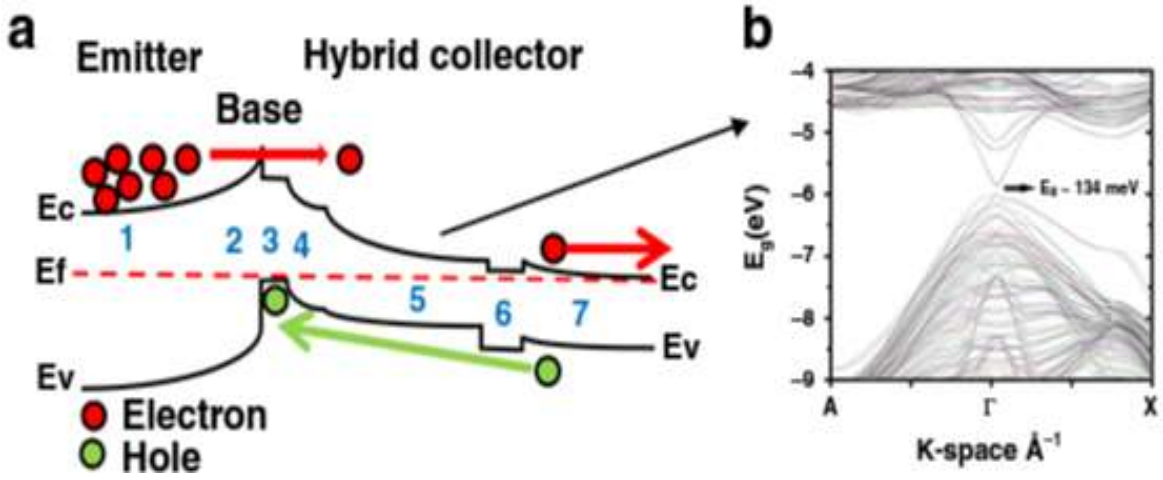

Figure 14. Energy band diagram and band structure of the HPT LWIR phototransistor device. a Schematic diagram of the conduction (E_C) and valence (E_V) bands of blue numbers 1–7 indicating the sectors of the device. b Band structure of the LWIR collector (sector 5) around the Γ-point calculated from the ETBM simulation with a bandgap of ~134meV.

Table 4. The bandgap of each sector as calculated by the ETBM.

Sector	1–2	3	4	5	6	7
Bandgap	635 meV	310 meV	310 meV	134 meV	166 meV	140 meV

The 60nm thick p-type base region (sector 3) is placed between the bottom n-contact/emitter (sectors 1 and 2) as the electron injector and the hybrid collector (sectors 4 and 5). The n-type emitter consists of a T2SL with 7/1/5/1 monolayers (MLs) of InAs/GaSb/AlSb/GaSb, respectively. The strain is controlled by using binary InSb for one interface and InGaSb for the other. The narrow-bandgap p-type base consists of 6.5/10 MLs of InAs/GaSb with a bandgap of ~310meV. As shown in Table. 4, the emitter (sector 2) has a much wider (~635 meV) bandgap with a precisely engineered valence band offset to the p-type base (sector 3) regardless of the doping concentration; using the ETBM, the emitter-base valence band offset was calculated to be ~303meV. This heterojunction between the emitter and base permits sufficient injection efficiency (high optical gain) from the emitter to the base while blocking reverse carrier injection from the base into the emitter. The abrupt junction between the narrow-band p-doped base and the narrow-band n-doped collector could trigger leakage current due to the reduction in the depletion width at this p-n junction, leading to enhancement of the electric field and causing band-to-band tunneling. To address this issue, an n-type hybrid T2SL-based collector structure was designed using the ETBM. Abutting the base is a lightly doped (n-type) 250nm thick region (sector 4) consisting of 6.5/10 MLs of InAs/GaSb with the same 310meV bandgap as in the base. Next comes a 1.0 μm thick n-doped narrow-bandgap LWIR part (sector

5) with 13/6 MLs of InAs/GaSb T2SL and a bandgap of ~134meV. The full band structure of this LWIR absorption region, as simulated by the ETBM, is shown in Fig. 2b. The last part of the design is the electron extractor region (sectors 6 and 7). Using the band structure engineering capabilities of T2SL, this extractor creates a barrier in the valence band embedded between the collector and top n-contact. This hole barrier (sector 6) is 250 nm thick and consists of a T2SL with 18/3/4/3 MLs of InAs/ GaSb/AlSb/GaSb; it has a bandgap of 166meV with a valence band offset of ~100meV with respect to the LWIR collector. Sector 7 is then a 200nm thick top highly doped n-contact that will extract all the electrons and has a structure with 13/7 MLs of InAs/GaSb and a bandgap of 140meV. The combination of sectors 6 and 7 allows efficient extraction of the electrons while blocking the transport of holes into the n-contact. This device is designed to have a floating base where the photodetector absorption region is the collector, which is coupled directly to the base without the need for external contact to bias the base. This floating base design simplifies the fabrication of the device and, more importantly, permits direct illumination of the collector. Incident LWIR light is absorbed in the LWIR portion of the collector (sector 5), leading to the generation of electron/ hole pairs. These carriers are then separated according to their minority carrier diffusion lengths in the collector and base and then swept away by the built-in electric field at the base–collector junction. Because this design uses a much wider bandgap material for the emitter, there is a potential barrier in the valence band at the emitter-base junction (sectors 2 and 3) that serves to stop the generated holes from entering the emitter. Holes, therefore, accumulate in the base region, modulating the base potential and thereby forward biasing the emitter–base junction. This, in turn, modulates the electron barrier between the emitter and base, which allows electrons from the emitter to overpass the base region and enter the collector. The use of a wide bandgap emitter can provide an emitter–base injection efficiency close to unity, regardless of the relative base/ emitter doping levels, since the valence band barrier effectively prevents hole injection from the base to the emitter. The injected electrons coming from the emitter can preserve the charge neutrality in the base region and maintain the large electron current flow toward the collector, which is the source of the transistor action and high gain of this LWIR HPT.

No anti-reflection coatings were applied to the devices. All measurements were done at 77 K. Under 220 mV of applied bias, the responsivity reached a peak value of 1284 A/W at ~6.8 μm (Fig. 15a). The 1/e cut-off wavelength of the device was 8.0 μm at 77 K. At applied biases (V_b) less than 220 mV, the responsivity at 6.8 μm decreased (Fig. 15b), and above 220 mV, the responsivity saturated. This strong dependence of the responsivity on the applied bias was related to the recombination rate in the base. At lower biases, electrons injected from the emitter spent more time in the base, which increased the probability that they would recombine with the holes that modulated the base transconductance—this amplified the effect of recombination in the base. Increasing the applied bias increased the electric field in the base region, leading to a higher drift velocity and a lower probability of recombination and thus a longer lifetime of the holes that modulate the transconductance of the base and an overall higher gain.

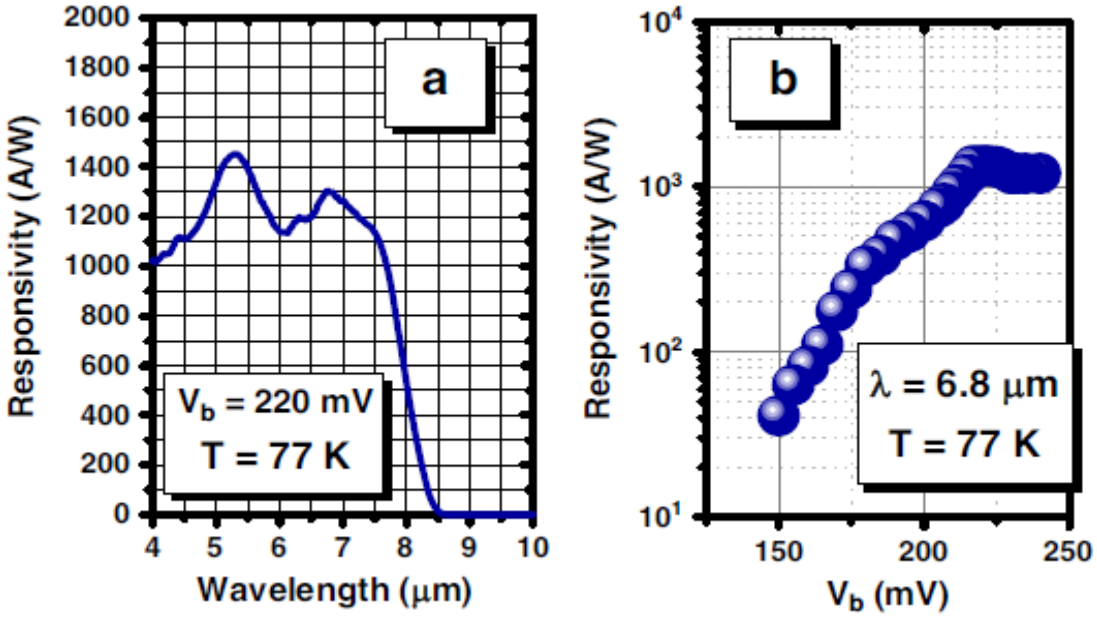

Figure 15. Optical performance of the LWIR T2SL phototransistor. a Saturated responsivity spectra of the device at 77K and V_b=220mV. b The variation in the responsivity at 6.8μm versus the applied bias voltage (V_b).

A 77 K cold shield was installed in a cryostat, and the dark current density and differential resistance-area product (R*A) versus V_b of a 200 μm diameter device were measured at 77 K (Fig. 16). The differential resistance-area product at zero bias was 1.2×10^7 Ωcm^2. Unity optical gain occurred at an applied bias of 129 mV, at which point the dark current density was 1.79×10^{-6} A/cm^2. By 220 mV, when the responsivity saturated, the dark current density had increased to 3.2×10^{-3} A/cm^2. The variation in the photocurrent generation at different temperatures is shown in Fig. 16c. The photocurrent follows an exponential trend and saturates in the range of ~10^{-3} A/cm^2. Illumination was performed using a helium–neon (HeNe) laser with 5.0mW of power. The DC current gain (β) of the device was experimentally calculated via comparison to a reference sample. The reference LWIR sample was grown by molecular beam epitaxy (MBE) and processed in the same way, but the layer sequence omitted the emitter/injector part (sectors 1 and 2) to prevent the phototransistor gain. This reference device at 77 K exhibits a saturated responsivity of 1.54 A/W at 6.8 μm, which corresponds to an external QE of η = 0.35. Dividing the saturated responsivity of the phototransistors by the saturated responsivity of the reference sample yields an experimentally estimated DC current gain (β) of 833. The optical gain of the device was also experimentally calculated directly from the saturated 6.8 μm responsivity measurements and from the calculation of the flux from the 1000 °C blackbody source.

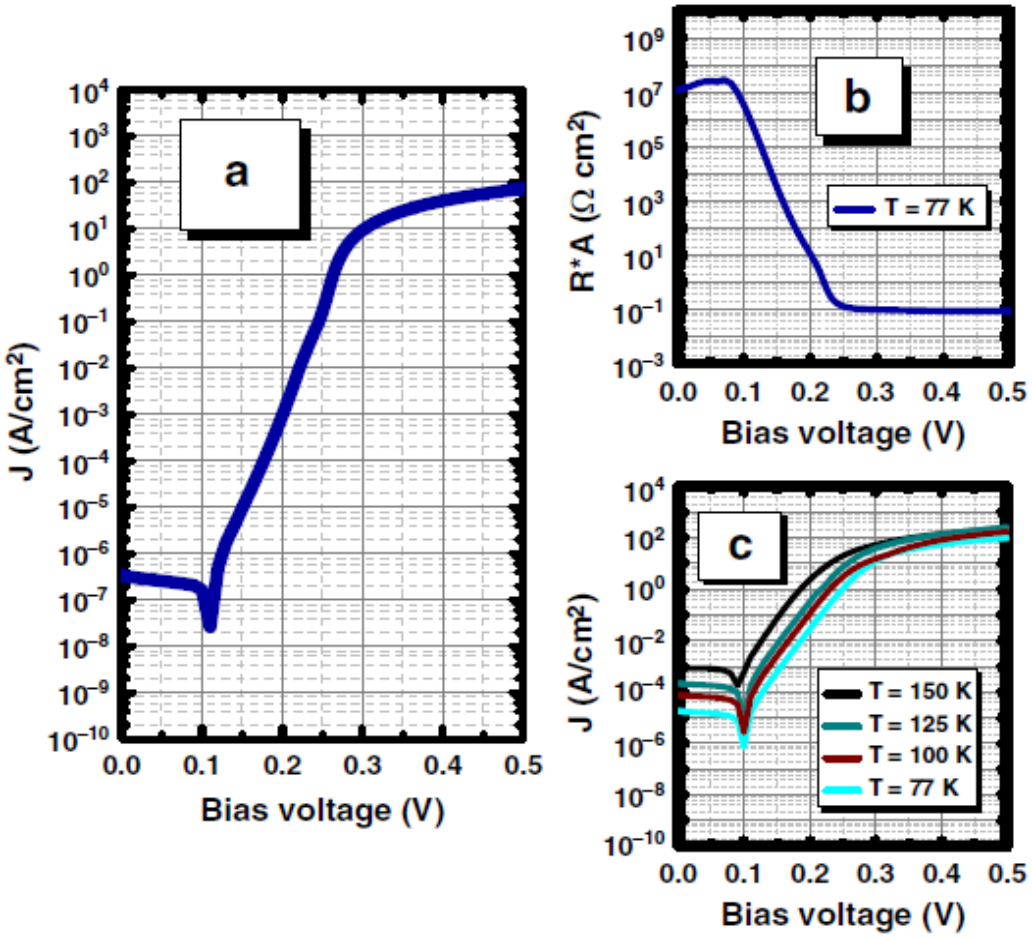

Figure 16. Electrical performance of the LWIR T2SL phototransistor. a Dark current density curves of the photodetector; b differential resistance-area product (R*A) at 77K vs. the applied bias voltage (V_b); and c variation in the photocurrent generation at different temperatures (77–150 K).

Optical gain is defined as the ratio of the number of carriers generated in the photocurrent to the number of coming incident photons. In practice, this approach means that we assume that the QE $\eta = 1.0$ (which is significantly higher than the $\eta = 0.35$ estimated from the reference device) and then simply normalize the responsivity to calculate the optical gain. The optical gain is directly proportional to the applied bias and increases with increasing V_b. The optical gain of the device saturates at a value of 276 at V_b greater than 220 mV and decreases to unity at $V_b = 90$ mV. To better understand the potential for low-light operation, the optical gain at 6.8 μm was measured at various incoming optical powers spanning over 4 decades (Fig. 17). To achieve this measurement, the device bias was maintained at $V_b = 220$ mV (saturated responsivity), and the blackbody temperature was changed from 1000 °C down to 100 °C to vary the incident optical power. No significant variation in the optical gain was observed over the 4-decade decrease in incoming optical power. This high dynamic range of performance is promising for LWIR applications with photon starvation or very low light levels.

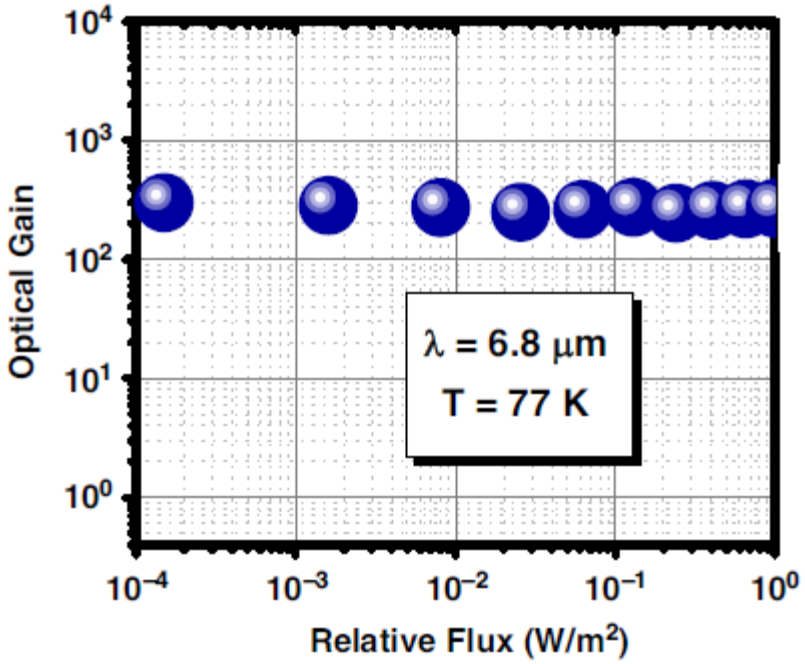

Figure 17. The optical gain of the LWIR phototransistor versus the relative incident optical power at 6.8 μm (T = 77 K and V_b = 220 mV).

7. CONCLUSION

In the project, the effect of several device parameters such as emitter doping concentration, base doping concentration, base thickness and energy bandgap difference between emitter and base on the optical gain of the T2SLs-based HPTs have been investigated and demonstrated. By reducing the base thickness to 20 nm, the optical gain of the HPT at 1.6 μ m saturates at 345.3. Also, we have reported the temperature dependence performance of e-SWIR HPT device for different size (15 μm and 10 μm diameter size). For 10 μm diameter circular diode, the -3dB cut-off frequency was measured to be 1.8 GHz -3dB, at room temperature with -20 V bias voltage. At 250K, the result showed that the speed improved a bit up to 2.2 GHz probably due to have lower dark current. The novel device structure, resonant cavity enhanced heterojunction phototransistor based on type-II superlattices grown by MBE has been demonstrated. The wavelength selectivity and a cavity enhancement of the responsivity at 1.9 μm were observed by introducing an eleven-pair lattice matched GaSb-AlAsSb Bragg reflector to form RCE structure. The responsivity for the RCE-HPT with an 80-nm collector layer reaches a peak value of 24.9 A/W at 1.9 μm under 2.5 V. The further improvement of the device structure and adding the high reflectivity top mirror can be implemented to realize the full potential of the RCE-HPT devices. We also demonstrated the design, growth, and characterization of a high-gain band-structure-engineered LWIR heterojunction phototransistor based on type-II superlattices. The 1/e cut-off wavelength of the device is 8.0 μm. At 77 K, unity optical gain occurs at a 90mV applied bias with a dark current density of 3.2×10^{-7} A/cm^2. The optical gain of the device at 77 K saturates at a value of 276 at an applied bias of 220 mV. The type-II superlattice-based high-gain LWIR device demonstrated our research effort to explore the possibility of implementing the band structure engineering method to develop the high-optical gain heterojunction phototransistors based on T2SLs.

8. REFERENCES

[1] A. Dehzangi, R. McClintock, D. H. Wu, A. Haddadi, R. Chevallier, and M. Razeghi, "Extended short wavelength infrared heterojunction phototransistors based on type II superlattices," (in English), *Appl Phys Lett,* vol. 114, no. 19, May 13 2019. [Online]. Available: <Go to ISI>://WOS:000470152800023.

[2] A. Dehzangi, A. Haddadi, S. Adhikary, and M. Razeghi, "Impact of scaling base thickness on the performance of heterojunction phototransistors," *Nanotechnology,* vol. 28, no. 10, p. 10LT01, 2017/02/02 2017, doi: 10.1088/1361-6528/aa5849.

[3] J. Li, A. Dehzangi, and M. Razeghi, "Performance analysis of infrared heterojunction phototransistors based on Type-II superlattices," *Infrared Phys Techn,* vol. 113, p. 103641, 2021/03/01/ 2021, doi: https://doi.org/10.1016/j.infrared.2021.103641.

[4] J. Li, A. Dehzangi, D. Wu, R. McClintock, and M. Razeghi, "Resonant cavity enhanced heterojunction phototransistors based on Type-II superlattices," *Infrared Phys Techn,* p. 103552, 2020/10/27/ 2020, doi: https://doi.org/10.1016/j.infrared.2020.103552.

[5] J. Li, A. Dehzangi, D. Wu, R. McClintock, and M. Razeghi, "Type-II superlattice-based heterojunction phototransistors for high speed applications," *Infrared Phys Techn,* vol. 108, p. 103350, 2020/08/01/ 2020, doi: https://doi.org/10.1016/j.infrared.2020.103350.

[6] A. Dehzangi *et al.*, "High speed antimony-based superlattice photodetectors transferred on sapphire," (in English), *Appl Phys Express,* vol. 12, no. 11, Nov 1 2019. [Online]. Available: <Go to ISI>://WOS:000502079100002.

[7] R. Chevallier *et al.*, "High Frequency Extended Short-Wavelength Infrared Heterojunction Photodetectors Based on InAs/GaSb/AlSb Type-II Superlattices," (in English), *Ieee J Quantum Elect,* vol. 54, no. 6, Dec 2018. [Online]. Available: <Go to ISI>://WOS:000448462100001.

[8] A. Perona *et al.*, "AlAsSb/GaSb doped distributed Bragg reflectors for electrically pumped VCSELs emitting around 2.3 mu m," (in English), *Semicond Sci Tech,* vol. 22, no. 10, pp. 1140-1144, Oct 2007, doi: 10.1088/0268-1242/22/10/010.

[9] D. Wu, J. Li, A. Dehzangi, and M. Razeghi, "Mid-wavelength infrared high operating temperature pBn photodetectors based on type-II InAs/InAsSb superlattice," *AIP Advances,* vol. 10, no. 2, p. 025018, 2020, doi: 10.1063/1.5136501.

PUBLICATIONS RELATED TO THE PROJECT

A. Dehzangi, J. Li, M. Razeghi, Band-structure-engineered high-gain LWIR photodetector based on type-II superlattice, Light: Science & Application, 10, 17 (2021); https://doi.org/10.1038/s41377-020-00453-x

J. Li, A. Dehzangi, M. Razeghi, Performance Analysis of Infrared Heterojunctionm Phototransistors based on Type-II Superlattices, Infrared Physics & Technology, 2020 (Accepted)

J. Li, D. Wu, A. Dehzangi, Ryan McClintock, M. Razeghi, Resonant cavity enhanced heterojunction phototransistors based on Type-II superlattices, Infrared Physics & Technology (2020), doi: https://doi.org/10.1016/j.infrared.2020.103552

J. Li, A. Dehzangi, D. Wu, M. Razeghi, 'Type-II superlattice-based heterojunction phototransistors for high-speed applications', Infrared Physics & Technology 108, 1033502 (2020)

Arash Dehzangi, Ryan McClintock, Donghai Wu, J. Li, Stephen Johnson, Emily Dial, Manijeh Razeghi, Appl. Phys. Express, 2019, 12 116502

A. Dehzangi, R. McClintock, D. H. Wu, A. Haddadi, R. Chevallier, and M. Razeghi, "Extended short wavelength infrared heterojunction phototransistors based on type II superlattices," (in English), Appl Phys Lett, vol. 114, no. 19, May 13 2019.

R. Chevallier et al., "High Frequency Extended Short-Wavelength Infrared Heterojunction Photodetectors Based on InAs/GaSb/AlSb Type-II Superlattices," (in English), Ieee J Quantum Elect, vol. 54, no. 6, Dec 2018.

A. Dehzangi, A. Haddadi, S. Adhikary, and M. Razeghi, "Impact of scaling base thickness on the performance of heterojunction phototransistors," Nanotechnology, vol. 28, no. 10, p. 10LT01, 2017/02/02 2017, doi: 10.1088/1361-6528/aa5849.

Abbas Haddadi, Arash Dehzangi, Romain Chevallier, Thomas Yang, Manijeh Razeghi, "Type-II InAs/GaSb/AlSb superlattice-based heterojunction phototransistors: back to the future," Proc. SPIE 10540, Quantum Sensing and Nano Electronics and Photonics XV, 1054004 (26 January 2018); doi: 10.1117/12.2297475

A. Haddadi, S. Adhikary, A. Dehzangi, and M. Razeghi , "Mid-wavelength infrared heterojunction phototransistors based on type-II InAs/AlSb/GaSb superlattices", Appl. Phys. Lett. 109, 021107 (2016) https://doi.org/10.1063/1.4958715

LIST OF SYMBOLS, ABBREVIATIONS, AND ACRONYMS

A ..... Ampere
A/W ..... Ampere/Watt
AC ..... Alternating-current
AFM ..... Atomic Force Microscopy
AFRL ..... Air Force Research Laboratory
Al ..... Aluminum
AlAsSb ..... Aluminum Arsenide Antimonide
AlSb ..... Aluminum Antimonide
APDs ..... Avalanche Photodiodes
As ..... Arsenide
Au ..... Gold
Be ..... Beryllium
BJT ..... Bipolar Junction Transistor
CF4 ..... Carbon Tetrafluoride
cm ..... Centimeter
dB ..... Decibel
DC ..... Direct-current
E_C ..... Conduction band
ECR ..... Electron Cyclotron Resonance
E_V ..... Valence band
e-SWIR ..... Extended-Sort wavelength infra-red
ETBM ..... Empirical Tight-Binding Method
Ga ..... Gallium
GaSb ..... Gallium Antimonide
GHz ..... Gigahertz
G-S-G ..... Ground-Signal-Ground
He-Ne ..... Helium-Neon
HPTs ..... Heterojunction Phototransistors
HR-XRD ..... High-Resolution X-ray Diffraction
ICP ..... Inductive coupled plasma
In ..... Indium
InAs ..... Indium Arsenide
InSb ..... Indium Antimonide
InAsSb ..... Indium Arsenide Antimonide
K ..... Kelvin
LIDAR ..... Light Detection and Ranging
LWIR ..... Long wavelength infra-red
MBE ..... Molecular Beam Epitaxy
MLs ..... Monolayers
mm-wave ..... millimeter-wave
NIR ..... Near infra-red
nm ..... Nanometer

PECVDPlasma assisted chemical vapor deposition
QE ..... Quantum Efficiency
R ..... Resistance
R*A ..... Differential resistance area product
RADAR ..... Radio Detection and Ranging
RCE-HPT ..... Resonant Cavity Enhanced Heterojunction Phototransistor
RF ..... Radio Frequency
RIE ..... Reactive ion etching
RXAN ..... Nanoelectronic Materials Branch, Functional Materials Division, Materials and ..... Manufacturing Directorate
Sb ..... Antimony
SEM ..... Scanning Electron Microscope
Si ..... Silicon
SiO2Silicon dioxide
SSMBE ..... Solid-Source Molecular Beam Epitaxy
SWIR ..... Sort wavelength infra-red
T2SL ..... Type-II superlattice
Te ..... Tellurium
Ti ..... Titanium
W ..... Watt
WPAFB ..... Wright-Patterson Air Force Base
µm ..... Micrometer
Å ..... Angstrom
λ ..... Lambda
β ..... Beta